Progress In Electromagnetics Research M, Vol. 97, 1–12, 2020

Microwave Staring Correlated Imaging Based on Quasi-Stationary Platform with Motion Measurement Errors

Zheng Jiang*, Bo Yuan, Jianlin Zhang, Yuanyue Guo, and Dongjin Wang

Abstract—Microwave staring correlated imaging (MSCI) is a promising technique for remote sensing due to its ability to achieve high-resolution microwave imaging without the limitation of relative motion between target and radar. In practical applications, unsteady quasi-stationary platforms, such as tethered aerostat, are often used as carriers of MSCI radar. However, these platforms cannot keep ideally stationary during the imaging process. The platform's motion caused by atmospheric effects will cause time-varying inaccuracy of observation positions. Although navigation systems can measure the platform's motion to compensate for the errors of observation positions, the imaging performance of MSCI may still suffer from degradation due to the measurement errors of navigation systems since MSCI is sensitive to model error. This paper focuses on MSCI based on the quasi-stationary platform with motion measurement errors. First, the MSCI model based on the quasi-stationary platform with motion measurement errors is established under the assumption that the translation and the rotation of the platform are uniform during a coherent imaging interval. Then we propose a self-calibration imaging method for MSCI based on the quasi-stationary platform with motion measurement errors. This method iterates over the steps of target reconstruction and motion measurement errors correction until convergent conditions are met. Simulation results show that the proposed method can correct the motion measurement errors and improve imaging performance significantly.

1. INTRODUCTION

Microwave staring correlated imaging (MSCI), motivated by classical coincidence imaging in optical systems, can achieve high-resolution imaging without relative motion between radar and target [1–3]. The essential principle of MSCI is to construct the temporal-spatial stochastic radiation field (TSSRF) in the imaging region, which is typically realized by a multi-transmitters configuration emitting independent stochastic modulated signal [4, 5]. By correlated imaging process (CIP), targets within the antenna beam could be distinguished.

In practical applications, to achieve continuous observation of critical areas, MSCI radar is often raised to a certain height by airborne quasi-stationary platforms, such as tethered aerostat. These quasi-stationary platforms cannot keep ideally stationary due to atmospheric effects. The unknown motion of the carrier platform will cause time-varying inaccuracy of observation positions and defocus the reconstructed image. Navigation systems, like the inertial navigation system (INS) and the global positioning system (GPS), can be used to measure the platform's motion. Due to the limited measurement accuracy, the measurement data is not completely accurate. Since MSCI depends on the precise observation model and is sensitive to the model error, the residual motion measurement errors may degrade the imaging performance of MSCI.

Received 18 June 2020, Accepted 11 September 2020, Scheduled 1 October 2020

* Corresponding author: Zheng Jiang (jiangz10@mail.ustc.edu.cn).

The authors are with the Key Laboratory of Electromagnetic Space Information, Chinese Academy of Sciences, University of Science and Technology of China, Hefei 230027, China.

Many studies have investigated the motion error problem in the field of airborne SAR imaging. A combination of the inertial navigation system (INS)/global positioning system (GPS)-based approach and the data-driven autofocus approach is usually employed to eliminate the motion errors in airborne SAR [6–9]. However, these methods cannot be applied to MSCI since the observation model of MSCI is different from SAR. For the model error problem in MSCI, most research focuses on the gain-phase error [10–13], off-grid error [14, 15], antenna position error [16] and target-motion-induced error [17] in MSCI based on the stationary platform. Few studies are concentrated on the errors caused by the motion of the platform. As far as we know, only [18] proposes to compensate for the motion errors by the polynomial fitting of the data of the position and orientation system (POS). The study also points out that MSCI is sensitive to motion measurement errors. Since MSCI based on the quasi-stationary platform is an essential issue in practical applications, it should be further investigated.

In this paper, we focus on MSCI based on the quasi-stationary platform with motion measurement errors. First, the MSCI model based on the quasi-stationary platform with motion measurement errors is established under the assumption that the translation and the rotation of the platform are uniform during a coherent imaging interval. The assumption is reasonable because a coherent imaging interval is usually very short. Then a joint target reconstruction and motion measurement errors correction method is proposed. The method involves an iterative algorithm that cycles through target reconstruction and motion measurement errors correction. The target image is recovered by Tikhonov regularization, and the motion measurement errors are corrected by the Newton method at each iteration. Compared with [18], this paper not only uses POS data to compensate for the motion errors, but also proposes a self-calibration imaging algorithm to estimate and correct the measurement errors. Therefore, the imaging performance of MSCI based on quasi-stationary platform is improved.

The rest of this paper is organized as follows. Section 2 presents the MSCI model based on the quasi-stationary platform. In Section 3, a joint target reconstruction and motion measurement errors correction method is proposed. In Section 4, numerical simulations are conducted to verify the effectiveness of the method. Finally, Section 5 concludes this paper.

2. MSCI MODEL BASED ON QUASI-STATIONARY PLATFORM

In this paper, MSCI based on the quasi-stationary platform is considered. Fig. 1 illustrates the imaging scene. The established Cartesian coordinate system O-XYZ is independent of the platform's motion. A quasi-stationary platform carries the MSCI radar system consisting of N transmitters and one receiver. The navigation systems are mounted in the center of the antenna array to dynamically measure the motion parameters of the antenna array. All transmitters emit stochastic modulated signals simultaneously to construct the TSSRF in the imaging region. The signal from the n-th transmitter is

$$s_n(t) = \sum_{q=1}^{Q} u\left[t-(q-1)T\right] \exp\left\{j2\pi f_{nq}\left[t-(q-1)T\right]\right\} \tag{1}$$

where f_{nq} is the frequency of the q-th pulse transmitted by the n-th transmitter. T is the pulse period. $u(t) = \mathrm{rect}(t/T_p)$ is the rectangular function. T_p is pulse width. Q is the number of pulses in a coherent processing interval.

The motion of the antenna array is decomposed into translation and rotation. The assumption that the translation and the rotation of the antenna array are uniform during a coherent imaging interval is made based on the fact that a coherent imaging interval is usually very short. The translation speed of the antenna array is denoted as $\mathbf{v} = [v_x, v_y, v_z]^T$, where v_x, v_y and v_z are the translation speed components along the X, Y and Z-axis, respectively. The rotation angular velocity of the antenna array is denoted as $\boldsymbol{\omega} = [\omega_x, \omega_y, \omega_z]^T$, where ω_x, ω_y and ω_z are the rotation angular velocity components around the X, Y, and Z-axis, respectively.

Matrix $\boldsymbol{\Omega}$ is defined as

$$\boldsymbol{\Omega} = \begin{bmatrix} 0 & -\omega_z & \omega_y \\ \omega_z & 0 & -\omega_x \\ -\omega_y & \omega_x & 0 \end{bmatrix} \tag{2}$$

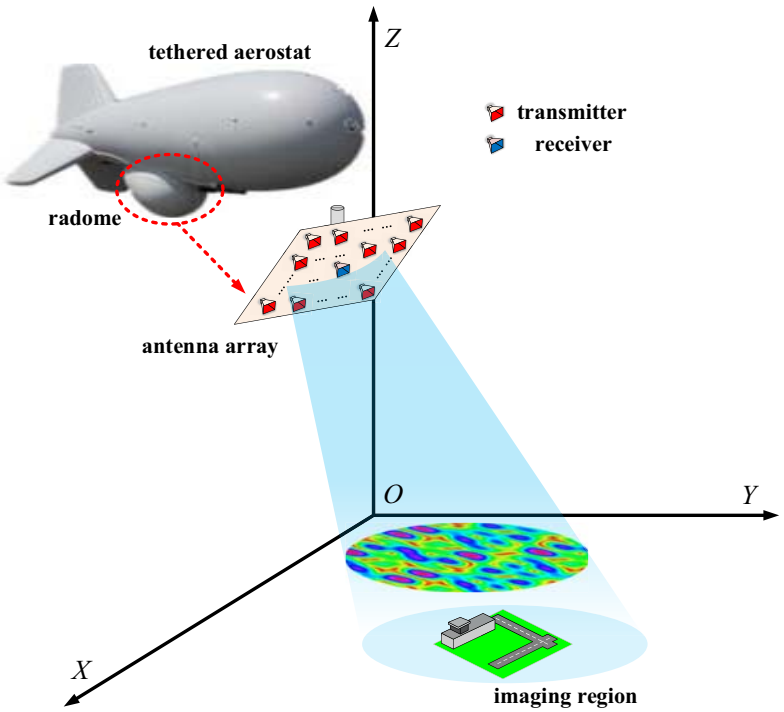

Figure 1. The imaging scene of MSCI based on the quasi-stationary platform.

The rotation matrix $\mathbf{R}_{ro}(t)$ can be expressed as

$$\mathbf{R}_{ro}(t) = \exp\left(\omega\hat{\mathbf{\Omega}}t\right) = \mathbf{I} + \hat{\mathbf{\Omega}}\sin(\omega t) + \hat{\mathbf{\Omega}}^2(1-\cos(\omega t)) \tag{3}$$

where $\hat{\mathbf{\Omega}} = \mathbf{\Omega}/\omega$ and $\omega = \|\boldsymbol{\omega}\|_2$.

Supposing that the receiver is located at the array center, its position vector at t is

$$\mathbf{r}_0(t) = \|\mathbf{r}_0(0) + \mathbf{v}t\| \tag{4}$$

where $\mathbf{r}_0(0)$ is the position vector of the receiver at the beginning of the imaging process.

The position vector of the n-th transmitter at t can be written as

$$\mathbf{r}_n(t) = \left\|\mathbf{r}_0(0) + \mathbf{v}t + \mathbf{R}_{ro}(t)\cdot\mathbf{r}'_n(0)\right\| \tag{5}$$

where $\mathbf{r}'_n(0) = \mathbf{r}_n(0) - \mathbf{r}_0(0)$. $\mathbf{r}_n(0)$ is the position vector of the n-th transmitter at the beginning of the imaging process.

The received echo can be described as

$$Sr(t) = \sum_{l=1}^{L}\sum_{n=1}^{N}\sigma_l s_n\left[t - \tau_n^l(t)\right] + w(t) \tag{6}$$

where $w(t)$ is the additive noise following Gaussian distribution. $\tau_n^l(t)$ is the propagation delay from the n-th transmitter to the receiver reflected by the target in the l-th imaging cell, and $t'_{nl} = t - \tau_n^l(t)$ is the transmission time of the n-th transmitter with respect to the reception time t and the propagation delay $\tau_n^l(t)$.

The propagation delay $\tau_n^l(t)$ can be expressed as

$$\begin{aligned}\tau_n^l(t) &= \frac{\|\mathbf{r}_l - \mathbf{r}_n(t'_{nl})\| + \|\mathbf{r}_0(t) - \mathbf{r}_l\|}{c} \\ &= \frac{\|\mathbf{r}_l - \mathbf{r}_0(0) - \mathbf{v}t'_{nl} - \mathbf{R}_{ro}(t'_{nl})\cdot\mathbf{r}'_n(0)\| + \|\mathbf{r}_0(0) + \mathbf{v}t - \mathbf{r}_l\|}{c}\end{aligned} \tag{7}$$

where $\mathbf{r}_l$ is the position vector of the l-th imaging cell. c is the light speed.

Assuming that the rotation angle of the antenna array is small during a coherent imaging interval, the rotation matrix can be approximated as $\mathbf{R}_{ro}(t) = \mathbf{I} + \mathbf{\Omega} t$. Thus the propagation delay $\tau_n^l(t)$ can be approximately written as

$$\tau_n^l(t) = \frac{\|\mathbf{r}_l - \mathbf{r}_n(0) - \mathbf{v}t'_{nl} - \mathbf{\Omega}\cdot\mathbf{r}'_n(0)\,t'_{nl}\| + \|\mathbf{r}_0(0) + \mathbf{v}t - \mathbf{r}_l\|}{c} \tag{8}$$

Since the imaging range is much larger than the size of the imaging region, the following approximations are made:

$$\left\|\mathbf{r}_l - \mathbf{r}_n(0) - \mathbf{v}t'_{nl} - \mathbf{\Omega}\cdot\mathbf{r}'_n(0)\,t'_{nl}\right\| \approx \|\mathbf{r}_l - \mathbf{r}_n(0)\| - \boldsymbol{\alpha}_{nl}\cdot\left(\mathbf{v}t'_{nl} + \mathbf{\Omega}\cdot\mathbf{r}'_n(0)\,t'_{nl}\right) \tag{9}$$

$$\|\mathbf{r}_0(0) - \mathbf{r}_l + \mathbf{v}t\| \approx \|\mathbf{r}_0(0) - \mathbf{r}_l\| + \boldsymbol{\alpha}_{lr}\cdot\mathbf{v}t \tag{10}$$

where $\boldsymbol{\alpha}_{nl}$ is the unit vector pointing from the n-th transmitter to the l-th imaging cell at the beginning of the imaging process; $\boldsymbol{\alpha}_{lr}$ is the unit vector pointing from the l-th imaging cell to the receiver at the beginning of the imaging process.

By substituting (9) and (10) into (8), we have

$$\tau_n^l(t) = \frac{\dfrac{\|\mathbf{r}_l - \mathbf{r}_n(0)\| + \|\mathbf{r}_0(0) - \mathbf{r}_l\|}{c} + \dfrac{(\boldsymbol{\alpha}_{lr} - \boldsymbol{\alpha}_{nl})\cdot\mathbf{v} - \boldsymbol{\alpha}_{nl}\cdot\mathbf{\Omega}\cdot\mathbf{r}'_n(0)}{c}t}{1 - \dfrac{\boldsymbol{\alpha}_{nl}\cdot(\mathbf{\Omega}\cdot\mathbf{r}'_n(0) + \mathbf{v})}{c}} \tag{11}$$

According to Taylor's expansion of Eq. (11) and the fact that the platform's speed is much lower than the light speed, the following expression is obtained

$$\begin{aligned}\tau_n^l(t) &= \frac{\|\mathbf{r}_l - \mathbf{r}_n(0)\| + \|\mathbf{r}_0(0) - \mathbf{r}_l\|}{c} + \frac{(\boldsymbol{\alpha}_{lr} - \boldsymbol{\alpha}_{nl})\cdot\mathbf{v} - \boldsymbol{\alpha}_{nl}\cdot\mathbf{\Omega}\cdot\mathbf{r}'_n(0)}{c}t \\ &= \tau_n^l(0) + \boldsymbol{\beta}_{nlr}\cdot\mathbf{v}t - \boldsymbol{\gamma}_{nl}\cdot\mathbf{\Omega}\cdot\mathbf{r}'_n(0)\,t\end{aligned} \tag{12}$$

where $\boldsymbol{\beta}_{nlr} = (\boldsymbol{\alpha}_{lr} - \boldsymbol{\alpha}_{nl})/c$ and $\boldsymbol{\gamma}_{nl} = \boldsymbol{\alpha}_{nl}/c$.

Assuming that $t = t_s + (q-1)T$, $(0 \le t_s \le T, 1 \le q \le Q)$, the echo of the q-th pulse has the following formula:

$$\begin{aligned}Sr(t) = \sum_{l=1}^{L}\sum_{n=1}^{N} &\sigma_l u\left(t_s - \tau_n^l(0) - \boldsymbol{\beta}_{nlr}\cdot\mathbf{v}t + \boldsymbol{\gamma}_{nl}\cdot\mathbf{\Omega}\cdot\mathbf{r}'_n(0)\,t\right)\cdot \\ &\exp\left(j2\pi f_{nq}\left(t_s - \tau_n^l(0) - \boldsymbol{\beta}_{nlr}\cdot\mathbf{v}t + \boldsymbol{\gamma}_{nl}\cdot\mathbf{\Omega}\cdot\mathbf{r}'_n(0)\,t\right)\right)\end{aligned} \tag{13}$$

Define the modified radiation field as

$$\begin{aligned}S(t, \mathbf{r}_l, \mathbf{v}, \boldsymbol{\omega}) = \sum_{n=1}^{N} &u\left[t_s - \tau_n^l(0) - \boldsymbol{\beta}_{nlr}\cdot\mathbf{v}t + \boldsymbol{\gamma}_{nl}\cdot\mathbf{\Omega}\cdot\mathbf{r}'_n(0)\,t\right]\cdot \\ &\exp\left(j2\pi f_{nq}\left(t_s - \tau_n^l(0) - \boldsymbol{\beta}_{nlr}\cdot\mathbf{v}t + \boldsymbol{\gamma}_{nl}\cdot\mathbf{\Omega}\cdot\mathbf{r}'_n(0)\,t\right)\right)\end{aligned} \tag{14}$$

Thus the echo can be reformulated as the superposition of the modified radiation field

$$Sr(t) = \sum_{l=1}^{L}\sigma_l S(t, \mathbf{r}_l, \mathbf{v}, \boldsymbol{\omega}) + w(t) \tag{15}$$

After sampling the received echo, the imaging equation can be formed as

$$\mathbf{Sr} = \mathbf{S}(\mathbf{v}, \boldsymbol{\omega})\cdot\boldsymbol{\sigma} + \mathbf{w} \tag{16}$$

where $\boldsymbol{\sigma} = [\sigma_1, \sigma_2, \cdots, \sigma_L]^T$ is the scattering coefficient vector. $\mathbf{w} = [w(t_1), w(t_2), \cdots, w(t_K)]^T$ is the noise vector. $\mathbf{Sr} = [Sr(t_1), Sr(t_2), \cdots, Sr(t_K)]^T$ is the echo vector. $\mathbf{S}(\mathbf{v}, \boldsymbol{\omega})$ is the sensing matrix which can be expressed as

$$\mathbf{S}(\mathbf{v}, \boldsymbol{\omega}) = \begin{bmatrix} S(t_1, \mathbf{r}_1, \mathbf{v}, \boldsymbol{\omega}) & S(t_1, \mathbf{r}_2, \mathbf{v}, \boldsymbol{\omega}) & \cdots & S(t_1, \mathbf{r}_L, \mathbf{v}, \boldsymbol{\omega}) \\ S(t_2, \mathbf{r}_1, \mathbf{v}, \boldsymbol{\omega}) & S(t_2, \mathbf{r}_2, \mathbf{v}, \boldsymbol{\omega}) & \cdots & S(t_2, \mathbf{r}_L, \mathbf{v}, \boldsymbol{\omega}) \\ \vdots & \vdots & \ddots & \vdots \\ S(t_K, \mathbf{r}_1, \mathbf{v}, \boldsymbol{\omega}) & S(t_K, \mathbf{r}_2, \mathbf{v}, \boldsymbol{\omega}) & \cdots & S(t_K, \mathbf{r}_L, \mathbf{v}, \boldsymbol{\omega}) \end{bmatrix} \tag{17}$$

In practice, the true motion parameters are unknown. We denote the measured translation speed and rotation angular velocity as $\mathbf{v}_m$ and $\boldsymbol{\omega}_m$, respectively. The measurement errors are denoted as $\mathbf{v}_e = \mathbf{v} - \mathbf{v}_m$ and $\boldsymbol{\omega}_e = \boldsymbol{\omega} - \boldsymbol{\omega}_m$. The imaging equation involving motion measurement errors can be written as

$$\mathbf{Sr} = \mathbf{S}_e\left(\mathbf{v}_e, \boldsymbol{\omega}_e\right) \cdot \boldsymbol{\sigma} + \mathbf{w} \tag{18}$$

where $\mathbf{S}_e(\mathbf{v}_e, \boldsymbol{\omega}_e) = \mathbf{S}(\mathbf{v}_m + \mathbf{v}_e, \boldsymbol{\omega}_m + \boldsymbol{\omega}_e)$.

3. SELF-CALIBRATION IMAGING METHOD

Although the accuracy of navigation systems can achieve quite high at present, the imaging performance of MSCI may still suffer from degradation since MSCI is sensitive to the model error. Therefore, in addition to using the navigation systems' data to compensate for the motion deviation, a joint target reconstruction and measurement errors correction method is also proposed to reduce the residual errors. The measurement errors are estimated from the received echo during the correlated imaging process. The problem of joint target reconstruction and measurement errors correction is formed as an optimization problem which minimizes the objective function as follows:

$$J\left(\boldsymbol{\sigma}, \mathbf{v}_e, \boldsymbol{\omega}_e\right) = \left\|\mathbf{Sr} - \mathbf{S}_e\left(\mathbf{v}_e, \boldsymbol{\omega}_e\right) \cdot \boldsymbol{\sigma}\right\|^2 + \lambda\|\boldsymbol{\sigma}\|^2 \tag{19}$$

where $\|\boldsymbol{\sigma}\|^2$ is a regularization term easing the ill-posed condition in target reconstruction. λ is the regularization parameter which keeps a balance between the data fidelity term and the regularization term.

We can obtain the reconstructed target and the estimated errors by minimizing the objective function jointly with $\boldsymbol{\sigma}$, $\mathbf{v}_e$ and $\boldsymbol{\omega}_e$.

$$\left[\boldsymbol{\sigma}^*, {\mathbf{v}_e}^*, {\boldsymbol{\omega}_e}^*\right] = \underset{\boldsymbol{\sigma}, \mathbf{v}_e, \boldsymbol{\omega}_e}{\arg\min}\, J\left(\boldsymbol{\sigma}, \mathbf{v}_e, \boldsymbol{\omega}_e\right) \tag{20}$$

An alternating iterative minimization algorithm, which iterates with steps of target reconstruction and motion measurement errors correction, is used to minimize the objective function. The algorithm procedures are outlined as follows:

Algorithm 1 Joint target reconstruction and motion measurement errors correction

Input: $\mathbf{Sr}$, $\mathbf{v}_m$, $\boldsymbol{\omega}_m$;
Output: $\boldsymbol{\sigma}^*$

1: initial $i = 0$, $I_{\max}$, η, $\boldsymbol{\omega}_e^0 = \mathbf{0}$ and $\mathbf{v}_e^0 = \mathbf{0}$;
2: **repeat**
3: reconstruct the target image: $\boldsymbol{\sigma}^i = \underset{\boldsymbol{\sigma}}{\arg\min}\, J\left(\boldsymbol{\sigma}, \mathbf{v}_e^{i-1}, \boldsymbol{\omega}_e^{i-1}\right)$;
4: estimate the error of translation speed: $\mathbf{v}_e^i = \underset{\mathbf{v}_e}{\arg\min}\, J\left(\boldsymbol{\sigma}^i, \mathbf{v}_e, \boldsymbol{\omega}_e^{i-1}\right)$;
5: estimate the error of rotation angular velocity: $\boldsymbol{\omega}_e^i = \underset{\boldsymbol{\omega}_e}{\arg\min}\, J\left(\boldsymbol{\sigma}^i, \mathbf{v}_e^i, \boldsymbol{\omega}_e\right)$;
6: update the sensing matrix: $\mathbf{S}_e\left(\mathbf{v}_e^i, \boldsymbol{\omega}_e^i\right)$;
7: **until** $\left(\left\|\boldsymbol{\sigma}^i - \boldsymbol{\sigma}^{i-1}\right\|^2 / \left\|\boldsymbol{\sigma}^{i-1}\right\|^2 < \eta \text{ or } i = I_{\max}\right)$

In the first step, we seek to recover the target image by minimizing the following objective function:

$$\boldsymbol{\sigma}^i = \arg\min_{\boldsymbol{\sigma}} \left\{\left\|\mathbf{Sr} - \mathbf{S}_e\left(\mathbf{v}_e^{i-1}, \boldsymbol{\omega}_e^{i-1}\right) \cdot \boldsymbol{\sigma}\right\|^2 + \lambda\|\boldsymbol{\sigma}\|^2\right\} \tag{21}$$

where the superscript represents the index of the iteration. Equation (21) is a Tikhonov regularization problem. The regularization parameter can be determined by the L-curve method. An explicit solution for $\boldsymbol{\sigma}$ is given by

$$\boldsymbol{\sigma}^i = \left[\mathbf{S}_e\left(\mathbf{v}_e^{i-1}, \boldsymbol{\omega}_e^{i-1}\right)^H \mathbf{S}_e\left(\mathbf{v}_e^{i-1}, \boldsymbol{\omega}_e^{i-1}\right) + \lambda\mathbf{I}\right]^{-1} \mathbf{S}_e\left(\mathbf{v}_e^{i-1}, \boldsymbol{\omega}_e^{i-1}\right)^H \mathbf{Sr} \tag{22}$$

In the steps of motion measurement errors correction, we first estimate the error of the translation speed by solving the following sub-problem:

$$\mathbf{v}_e^i = \arg\min_{\mathbf{v}_e} \left\{ \left\| \mathbf{Sr} - \mathbf{S}_e\left(\mathbf{v}_e, \boldsymbol{\omega}_e^{i-1}\right) \cdot \boldsymbol{\sigma}^i \right\|^2 + \lambda \left\| \boldsymbol{\sigma}^i \right\|^2 \right\} \tag{23}$$

As $\lambda\|\boldsymbol{\sigma}^i\|^2$ is a constant, Equation (23) can be rewritten as

$$\mathbf{v}_e^i = \arg\min_{\mathbf{v}_e} \left\| \mathbf{Sr} - \mathbf{S}_e\left(\mathbf{v}_e, \boldsymbol{\omega}_e^{i-1}\right) \cdot \boldsymbol{\sigma}^i \right\|^2 \tag{24}$$

Equation (24) is a nonlinear least-squares problem. We employ the Newton method to obtain the solution. The updating of $\mathbf{v}_e$ can be expressed as

$$\mathbf{v}_e^i = \mathbf{v}_e^{i-1} - \left[\nabla^2_{\mathbf{v}_e} J\left(\boldsymbol{\sigma}^i, \mathbf{v}_e^{i-1}, \boldsymbol{\omega}_e^{i-1}\right)\right]^{-1} \cdot \nabla_{\mathbf{v}_e} J\left(\boldsymbol{\sigma}^i, \mathbf{v}_e^{i-1}, \boldsymbol{\omega}_e^{i-1}\right) \tag{25}$$

where $\nabla_{\mathbf{v}_e} J(\boldsymbol{\sigma}^i, \mathbf{v}_e^{i-1}, \boldsymbol{\omega}_e^{i-1})$ and $\nabla^2_{\mathbf{v}_e} J(\boldsymbol{\sigma}^i, \mathbf{v}_e^{i-1}, \boldsymbol{\omega}_e^{i-1})$ are the gradient and the Hessian matrix of the objective function with respect to $\mathbf{v}_e$, respectively.

The updating of the angular velocity error, which is similar to the translation speed, can be described as

$$\boldsymbol{\omega}_e^i = \boldsymbol{\omega}_e^{i-1} - \left[\nabla^2_{\boldsymbol{\omega}_e} J\left(\boldsymbol{\sigma}^i, \mathbf{v}_e^{i}, \boldsymbol{\omega}_e^{i-1}\right)\right]^{-1} \cdot \nabla_{\boldsymbol{\omega}_e} J\left(\boldsymbol{\sigma}^i, \mathbf{v}_e^{i}, \boldsymbol{\omega}_e^{i-1}\right) \tag{26}$$

where $\nabla_{\boldsymbol{\omega}_e} J(\boldsymbol{\sigma}^i, \mathbf{v}_e^{i}, \boldsymbol{\omega}_e^{i-1})$ and $\nabla^2_{\boldsymbol{\omega}_e} J(\boldsymbol{\sigma}^i, \mathbf{v}_e^{i}, \boldsymbol{\omega}_e^{i-1})$ are the gradient and the Hessian matrix of the objective function with respect to $\boldsymbol{\omega}_e$, respectively.

The sensing matrix is updated with the new estimated parameters, and the convergence conditions are checked before passing to the next iteration. If $\|\boldsymbol{\sigma}^i - \boldsymbol{\sigma}^{i-1}\|^2 / \|\boldsymbol{\sigma}^{i-1}\|^2 < \eta$ or the maximum number of the iteration is reached, the algorithm is terminated.

The derivations of the gradients and the Hessian matrices are given in Appendix A.

4. NUMERICAL SIMULATIONS

In this section, numerical simulations are performed to verify the effectiveness of the proposed method. The simulation parameters are selected according to the possible scenarios in practical applications. A MSCI system consisting of 25 transmitters and one receiver is considered. The transmitters are configured as a 5×5 uniform 2-D rectangular array, and the receiver is in the array center. The working height of the tethered balloon is usually several hundred meters to several kilometers, so in the simulations the height of the platform is set to 280 m. Frequency-hopping signals are used as transmitted signals, and the frequency of each pulse is randomly selected within the signal bandwidth. The target shown in Fig. 2 is a ship and its sizes are set to 50 m × 20 m. The resolution of MSCI is set to 1 m, which demonstrates that MSCI is able to achieve high-resolution microwave imaging. The simulation parameters are shown in Table 1.

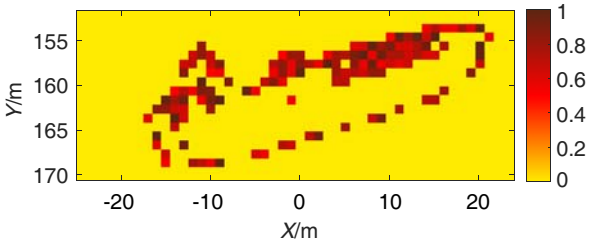

Figure 2. Target image.

4.1. Illustrative Example

In the subsection, an illustrative example is shown to prove the effectiveness of the proposed method. As the platform is quasi-stationary, the maximum value of the motion is not very large. The motion parameters of the platform are randomly selected within the maximum value. The maximum speed is

Table 1. Simulation parameters.

Simulation parameter	Value
Number of transmitters	25
Aperture of antenna array	$2\,\mathrm{m} \times 2\,\mathrm{m}$
Carrier frequency	9.6 GHz
Bandwidth	500 MHz
Slanting angle	30°
Number of grids	50×20
Grid spacing	1 m
Platform height	280 m
SNR	20 dB

set to 10 m/s and the maximum angular velocity is set to 10 rad/s. The maximum relative measurement errors are set to 10%.

The randomly generated translation speed and rotation angular velocity are $\mathbf{v} = [8.2\,\mathrm{m/s}, 9.7\,\mathrm{m/s}, 5.3\,\mathrm{m/s}]^T$ and $\boldsymbol{\omega} = [5.8\,\mathrm{rad/s}, -6.4\,\mathrm{rad/s}, 8.1\,\mathrm{rad/s}]^T$, respectively. The motion measurement errors are $\mathbf{v}_e = [0.5\,\mathrm{m/s}, -0.4\,\mathrm{m/s}, 0.5\,\mathrm{m/s}]^T$ and $\boldsymbol{\omega}_e = [0.3\,\mathrm{rad/s}, -0.4\,\mathrm{rad/s}, 0.6\,\mathrm{rad/s}]^T$. Fig. 3(a) shows the imaging result without errors correction. The target image is recovered by Tikhonov regularization. It can be seen that the image is blurry and defocused, and the profile of the target is hard to recognize. Fig. 3(b) shows the imaging result recovered by our proposed method. The reconstructed target is focused and accurate, which demonstrates that the proposed method can correct the measurement errors and improve the imaging performance effectively.

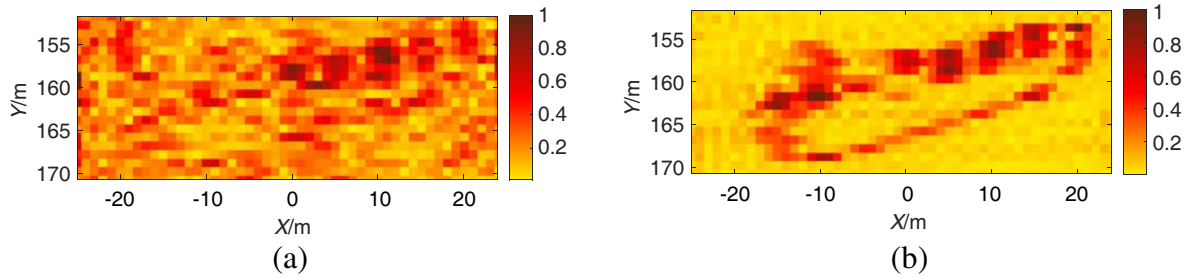

Figure 3. The imaging results. (a) The imaging result without motion measurement errors correction. (b) The imaging result recovered by our proposed method.

In order to provide a quantitative metric of the imaging quality, the relative imaging error (RIE) $\|\hat{\boldsymbol{\sigma}} - \boldsymbol{\sigma}\|_2 / \|\boldsymbol{\sigma}\|_2$, where $\boldsymbol{\sigma}$ is the original target image and $\hat{\boldsymbol{\sigma}}$ is the reconstructed target, is introduced. The curve of RIE versus iteration number is presented in Fig. 4. It can be seen that RIE decreases rapidly as the number of iterations increases, which shows that the iterative algorithm is efficient and fast convergent.

The speed error $\mathbf{v}_e$ causes a phase error in the received echo signal. The phase error can be expressed as $\exp(-j2\pi f_n \boldsymbol{\beta}_{nlr} \cdot \mathbf{v}_e t)$. The value of the phase error depends on the projection of the speed error $\mathbf{v}_e$ on the vector $\boldsymbol{\beta}_{nlr} = (\boldsymbol{\alpha}_{lr} - \boldsymbol{\alpha}_{nl})/c$. Thus we define the equivalent translation speed deviation $\theta(\mathbf{v}_e) = \|(\boldsymbol{\alpha}_{lr} - \boldsymbol{\alpha}_{nl}) \cdot \mathbf{v}_e\|_2$ to assess the phase error caused by the speed error $\mathbf{v}_e$. As $\boldsymbol{\alpha}_{lr} \approx \boldsymbol{\alpha}_r$ and $\boldsymbol{\alpha}_{nl} \approx -\boldsymbol{\alpha}_r$, where $\boldsymbol{\alpha}_r$ is a unit vector pointing from the center of the imaging area to the center of the antenna array, the equivalent translation speed deviation can be rewritten as $\theta(\mathbf{v}_e) = 2\|\boldsymbol{\alpha}_r \cdot \mathbf{v}_e\|_2$. Similar to the equivalent translation speed deviation, equivalent angular velocity deviation $\phi(\boldsymbol{\omega}_e) = \|\boldsymbol{\alpha}_r \cdot \boldsymbol{\Omega}(\boldsymbol{\omega}_e)\|$ is also introduced to assess the phase error caused by the measurement error of rotation angular velocity.

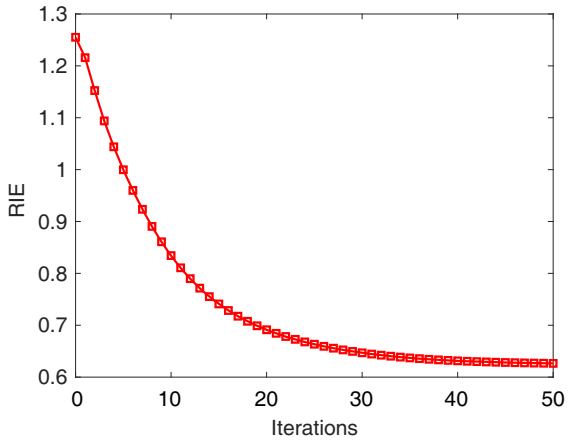

Figure 4. RIE versus the number of iterations.

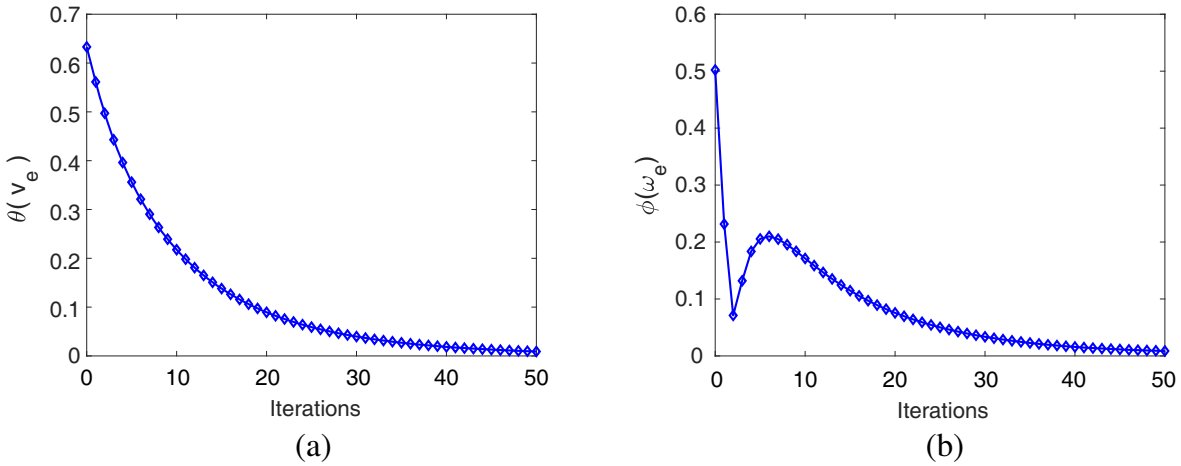

Figure 5. $\theta(\mathbf{v}_e)$ and $\phi(\boldsymbol{\omega}_e)$ versus the number of iterations. (a) $\theta(\mathbf{v}_e)$ versus the number of iterations. (b) $\phi(\boldsymbol{\omega}_e)$ versus the number of iterations.

Figure 5 presents that both $\theta(\mathbf{v}_e)$ and $\phi(\boldsymbol{\omega}_e)$ are nearly reduced to zero, which shows that our proposed method can correct the phase errors caused by the motion measurement errors.

4.2. Imaging Performance under Different SNRs

In this subsection, the imaging performance of our proposed method is evaluated under different SNRs by Monte Carlo simulation. The SNR varies from -10 dB to 40 dB with step of 5 dB. 100 independent experiments are performed under all SNRs, and the final result for each SNR is averaged over the 100 experiments. For each experiment, the translation speed and the rotation angular velocity are randomly generated with a maximum speed of 10 m/s and a maximum angular velocity of 10 rad/s. The relative measurement error for each motion component is distributed uniformly in $[-10\%, 10\%]$.

Figure 6 shows the imaging results under different SNRs, and Fig. 7 illustrates the RIE under different SNRs. It can be seen that the quality of the reconstructed target is reduced when SNR is low; however, when SNR is larger than 0 dB, the imaging performance of the proposed method is less affected by the noise. It may be explained by the fact that Tikhonov regularization increases the robustness of the proposed method to noise.

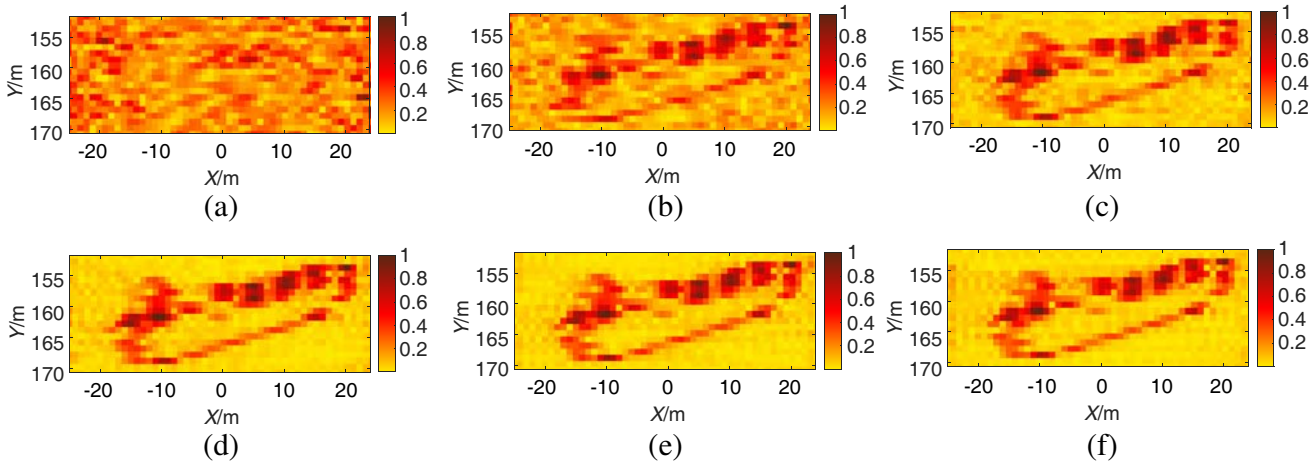

Figure 6. The imaging results under different SNRs. (a) SNR $= -10$ dB. (b) SNR $= 0$ dB. (c) SNR $= 10$ dB. (d) SNR $= 20$ dB. (e) SNR $= 30$ dB. (f) SNR $= 40$ dB.

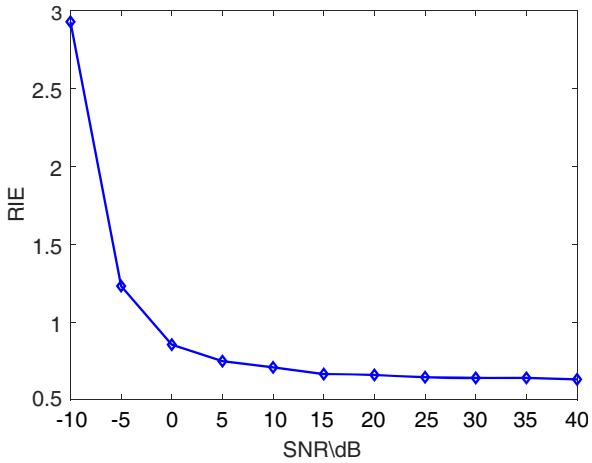

Figure 7. RIEs under different SNRs.

4.3. Imaging Performance under Different Target Scenes

To explore the influence of target texture on the imaging performance, simulations are conducted under different target scenes in this subsection. As shown in Figs. 8(a)–(c), three different target scenes are introduced for comparison. The simulation parameters are given in Table 1. The imaging results for different target scenes are shown in Fig. 8 and the RIEs of the proposed method for different target scenes under different SNRs are given in Table 2. Fig. 8 shows that the proposed method can obtain desirable imaging results for different target scenes. Table 2 shows that the RIEs for different target

Table 2. RIEs for different target scenes.

SNR	Target 1	Target 2	Target 3
0 dB	0.82	0.86	0.81
10 dB	0.69	0.70	0.71
20 dB	0.65	0.66	0.66

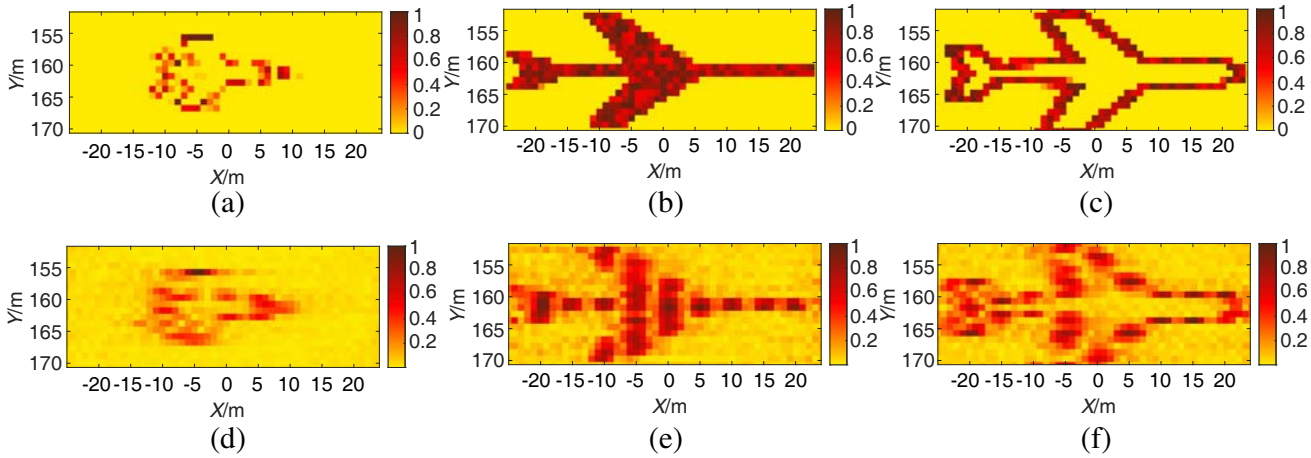

Figure 8. The imaging results for different target scenes. (a) Original target 1. (b) Original target 2. (c) Original target 3. (d) Reconstructed target 1 by the proposed method. (e) Reconstructed target 2 by the proposed method. (f) Reconstructed target 3 by the proposed method.

scenes are very close under the same signal-to-noise ratio. Therefore, we draw a conclusion that the imaging performance is almost unaffected by the target texture.

5. CONCLUSION

In this paper, we focus on MSCI based on the quasi-stationary platform with motion measurement errors. First, the MSCI model based on the quasi-stationary platform is established under the assumption that the translation and the rotation of the quasi-stationary platform are uniform during a coherent imaging interval. The imaging equation involving motion measurement errors is obtained according to the established MSCI model. Then a joint target reconstruction and motion measurement errors correction method is proposed. It uses an iterative algorithm, where each iteration consists of consecutive steps of target reconstruction and measurement errors correction. Numerical simulations show the effectiveness of our proposed method.

The establishment of the MSCI model in this paper depends on the assumption that the translation and the rotation are uniform during a coherent imaging interval. The assumption is reasonable for some cases; however, it is not suitable for all situations. Further efforts will be made for more general situations.

ACKNOWLEDGMENT

This work was supported by National Natural Science Foundation of China under Grant No. 61771446.

APPENDIX A.

In this appendix, the gradient and the Hessian matrix of the objective function are derived.

Assuming v_a $(1 \leq a \leq 3)$ is the a-th component of $\mathbf{v}_e$, the a-th element in $\nabla_{\mathbf{v}_e} J(\boldsymbol{\sigma}, \mathbf{v}_e, \boldsymbol{\omega}_e)$ can be expressed as

$$\frac{\partial J\left(\boldsymbol{\sigma}, \mathbf{v}_e, \boldsymbol{\omega}_e\right)}{\partial v_a} = -\boldsymbol{\sigma}^H \frac{\partial \mathbf{S}^H}{\partial v_a} \mathbf{S}\mathbf{r} - \mathbf{S}\mathbf{r}^H \frac{\partial \mathbf{S}}{\partial v_a} \boldsymbol{\sigma} + \boldsymbol{\sigma}^H \frac{\partial \mathbf{S}^H}{\partial v_a} \boldsymbol{S}\boldsymbol{\sigma} + \boldsymbol{\sigma}^H \mathbf{S}^H \frac{\partial \mathbf{S}}{\partial v_a} \boldsymbol{\sigma} \tag{A1}$$

The a-th diagonal element in Hessian matrix $\nabla^2_{\mathbf{v}_e} J(\boldsymbol{\sigma}, \mathbf{v}_e, \boldsymbol{\omega}_e)$ can be expressed as

$$\frac{\partial^2 J\left(\boldsymbol{\sigma}, \mathbf{v}_e, \boldsymbol{\omega}_e\right)}{\partial {v_a}^2} = -\boldsymbol{\sigma}^H \frac{\partial^2 \mathbf{S}^H}{\partial {v_a}^2} \mathbf{S}\mathbf{r} - \mathbf{S}\mathbf{r}^H \frac{\partial^2 \mathbf{S}}{\partial {v_a}^2} \boldsymbol{\sigma} + 2\boldsymbol{\sigma}^H \frac{\partial \mathbf{S}^H}{\partial v_a} \frac{\partial \mathbf{S}}{\partial v_a} \boldsymbol{\sigma} + \boldsymbol{\sigma}^H \frac{\partial^2 \mathbf{S}^H}{\partial {v_a}^2} \boldsymbol{S}\boldsymbol{\sigma} + \boldsymbol{\sigma}^H \mathbf{S}^H \frac{\partial^2 \mathbf{S}}{\partial {v_a}^2} \boldsymbol{\sigma} \tag{A2}$$

The expression of the element in row a and column b of the Hessian matrix $\nabla^2_{\mathbf{v}_e} J(\boldsymbol{\sigma}, \mathbf{v}_e, \boldsymbol{\omega}_e)$ is

$$\begin{aligned}\frac{\partial^2 J(\boldsymbol{\sigma}, \mathbf{v}_e, \boldsymbol{\omega}_e)}{\partial v_a \partial v_b} &= -\boldsymbol{\sigma}^H \frac{\partial^2 \mathbf{S}^H}{\partial v_a \partial v_b} \mathbf{S}\mathbf{r} - \mathbf{S}\mathbf{r}^H \frac{\partial^2 \mathbf{S}}{\partial v_a \partial v_b} \boldsymbol{\sigma} + \boldsymbol{\sigma}^H \frac{\partial \mathbf{S}^H}{\partial v_a} \frac{\partial \mathbf{S}}{\partial v_b} \boldsymbol{\sigma} \\ &\quad + \boldsymbol{\sigma}^H \frac{\partial^2 \mathbf{S}^H}{\partial v_a \partial v_b} \boldsymbol{S}\boldsymbol{\sigma} + \boldsymbol{\sigma}^H \frac{\partial \mathbf{S}^H}{\partial v_a} \frac{\partial \mathbf{S}}{\partial v_b} \boldsymbol{\sigma} + \boldsymbol{\sigma}^H \mathbf{S}^H \frac{\partial^2 \mathbf{S}}{\partial v_a \partial v_b} \boldsymbol{\sigma} \end{aligned} \tag{A3}$$

The expressions of the elements in $\nabla_{\boldsymbol{\omega}_e} J(\boldsymbol{\sigma}, \mathbf{v}_e, \boldsymbol{\omega}_e)$ and $\nabla^2_{\boldsymbol{\omega}_e} J(\boldsymbol{\sigma}, \mathbf{v}_e, \boldsymbol{\omega}_e)$ are the same with the corresponding elements in $\nabla_{\mathbf{v}_e} J(\boldsymbol{\sigma}, \mathbf{v}_e, \boldsymbol{\omega}_e)$ and $\nabla^2_{\mathbf{v}_e} J(\boldsymbol{\sigma}, \mathbf{v}_e, \boldsymbol{\omega}_e)$.

The gradient and the Hessian matrix of the objective function depend on the derivate and the second derivate of $\mathbf{S}$ with respect to the motion variable.

$$\frac{\partial \mathbf{S}(k,l)}{\partial v_a} = \sum_{n=1}^{N} -j2\pi f_{nk} \beta_{nl,a} t_k \exp\left(j2\pi f_{nk}\left(t_s - \tau_n^l(0) - \boldsymbol{\beta}_{nl} \cdot \mathbf{v} t_k + \boldsymbol{\gamma}_{nl} \cdot \boldsymbol{\Omega} \cdot \mathbf{r}'_n(0) t_k\right)\right) \tag{A4}$$

$$\frac{\partial^2 \mathbf{S}(k,l)}{\partial^2 v_a} = \sum_{n=1}^{N} \frac{(-j2\pi f_{nk} \beta_{nl,a} t_k)^2}{\exp\left(j2\pi f_{nk}\left(t_s - \tau_n^l(0) - \boldsymbol{\beta}_{nl} \cdot \mathbf{v} t_k + \boldsymbol{\gamma}_{nl} \cdot \boldsymbol{\Omega} \cdot \mathbf{r}'_n(0) t_k\right)\right)} \tag{A5}$$

$$\frac{\partial^2 \mathbf{S}(k,l)}{\partial v_a \partial v_b} = \sum_{n=1}^{N} \frac{(-j2\pi f_{nk} \beta_{nl,a} t_k)(-j2\pi f_{nk} \beta_{nl,b} t_k)}{\exp\left(j2\pi f_{nk}\left(t_s - \tau_n^l(0) - \boldsymbol{\beta}_{nl} \cdot \mathbf{v} t_k + \boldsymbol{\gamma}_{nl} \cdot \boldsymbol{\Omega} \cdot \mathbf{r}'_n(0) t_k\right)\right)} \tag{A6}$$

where $t_k = t_s + (k-1)T$, $(0 \le t_s < T)$ is the sampling time of the k-th pulse.

Supposing $\mathbf{r}'_n(0) = [r_x, r_y, r_z]^T$, $\rho_x = (-r_z\gamma_{nl,y} + r_y\gamma_{nl,z})$, $\rho_y = (-r_x\gamma_{nl,z} + r_z\gamma_{nl,x})$, and $\rho_z = (-r_y\gamma_{nl,x} + r_x\gamma_{nl,y})$, the derivate and the second derivate of $\mathbf{S}$ with respect to $\boldsymbol{\omega}$ can be written as

$$\frac{\partial \mathbf{S}(k,l)}{\partial \omega_a} = \sum_{n=1}^{N} j2\pi f_{nk} t_k \rho_a \exp\left(j2\pi f_{nk}\left(t_s - \tau_n^l(0) - \boldsymbol{\beta}_{nl} \cdot \mathbf{v} t_k + \boldsymbol{\gamma}_{nl} \cdot \boldsymbol{\Omega} \cdot \mathbf{r}'_n(0) t_k\right)\right) \tag{A7}$$

$$\frac{\partial^2 \mathbf{S}(k,l)}{\partial^2 \omega_a} = \sum_{n=1}^{N} -(2\pi f_{nk} t_k)^2 {\rho_a}^2 \exp\left(j2\pi f_{nk}\left(t_s - \tau_n^l(0) - \boldsymbol{\beta}_{nl} \cdot \mathbf{v} t_k + \boldsymbol{\gamma}_{nl} \cdot \boldsymbol{\Omega} \cdot \mathbf{r}'_n(0) t_k\right)\right) \tag{A8}$$

$$\frac{\partial^2 \mathbf{S}(k,l)}{\partial \omega_a \partial \omega_b} = \sum_{n=1}^{N} -(2\pi f_{nk} t_k)^2 \rho_a \rho_b \exp\left(j2\pi f_{nk}\left(t_s - \tau_n^l(0) - \boldsymbol{\beta}_{nl} \cdot \mathbf{v} t_k + \boldsymbol{\gamma}_{nl} \cdot \boldsymbol{\Omega} \cdot \mathbf{r}'_n(0) t_k\right)\right) \tag{A9}$$

REFERENCES

1. He, X., B. Liu, and D. Wang, "A novel approach of high spatial-resolution microwave staring correlated imaging," *Proceedings of 2013 Asia-Pacific Conference on Synthetic Aperture Radar*, 75–78, Tsukuba, Japan, September 2013.
2. Guo, Y., X. He, and D. Wang, "A novel super-resolution imaging method based on stochastic radiation radar array," *Measurement Science and Technology*, Vol. 24, No. 7, 31–36, 2013.
3. Li, D., X. Li, Y. Cheng, Y. Qin, and H. Wang, "Radar coincidence imaging: An instantaneous imaging technique with stochastic signals," *IEEE Transactions on Geoscience Remote Sensing*, Vol. 52, No. 4, 2261–2271, 2014.
4. Zhu, S., A. Zhang, Z. Xu, and X. Dong, "Radar coincidence imaging with random microwave source," *IEEE Antennas and Wireless Propagation Letters*, Vol. 14, 1239–1242, 2015.
5. Guo, Y., D. Wang, and C. Tian, "Research on sensing matrix characteristics in microwave staring correlated imaging based on compressed sensing," *2014 IEEE International Conference on Imaging Systems and Techniques (IST)*, 195–200, IEEE, 2014.
6. Zhang, L., J. Sheng, M. Xing, Z. Qiao, T. Xiong, and Z. Bao, "Wavenumber-domain autofocusing for highly squinted UAV SAR imagery," *IEEE Sensors Journal*, Vol. 12, No. 5, 1574–1588, 2012.

7. Fornado, G., "Trajectory deviations in airborne SAR: Analysis and compensation," *IEEE Transactions on Aerospace and Electronic Systems*, Vol. 35, No. 3, 997–1009, 1999.
8. Cao, N., H. Lee, E. Zaugg, R. Shrestha, and H. Yu, "Estimation of residual motion errors in airborne sar interferometry based on time-domain backprojection and multisquint techniques," *IEEE Transactions on Geoscience and Remote Sensing*, Vol. 56, No. 4, 2397–2407, 2018.
9. Yang, J., X. Huang, J. Thompson, T. Jin, and Z. Zhou, "Compressed sensing radar imaging with compensation of observation position error," *IEEE Transactions on Geoscience and Remote Sensing*, Vol. 52, No. 8, 4608–4620, 2014.
10. Zhou, X., H. Wang, Y. Cheng, et al., "Radar coincidence imaging with phase error using bayesian hierarchical prior modeling," *Journal of Electronic Imaging*, Vol. 25, No. 1, 013018, 2016.
11. Zhou, X., H. Wang, Y. Cheng, and Y. Qin, "Sparse auto-calibration for radar coincidence imaging with gain-phase errors," *Sensors*, Vol. 15, No. 11, 27611–27624, 2015.
12. Tian, C., B. Yuan, and D. Wang, "Calibration of gain-phase and synchronization errors for microwave staring correlated imaging with frequency-hopping waveforms," *Proceedings of the IEEE Radar Conference*, 1328–1333, 2018.
13. Xia, R., Y. Guo, W. Chen, and D. Wang, "Strip-mode microwave staring correlated imaging with self-calibration of gain-phase errors," *Sensors*, Vol. 19, No. 5, 1079, 2019.
14. Zhou, X., H. Wang, Y. Cheng, Y. Qin, and H. Chen, "Radar coincidence imaging for off-grid target using frequency hopping waveforms," *International Journal of Antennas and Propagation*, Vol. 2016, 1–16, 2016.
15. Zhou, X., H. Wang, Y. Cheng, and Y. Qin, "Off-grid radar coincidence imaging based on variational sparse Bayesian learning," *Mathematical Problems in Engineering*, Vol. 2016, 1782178, 2016.
16. Zhou, X., B. Fan, H. Wang, Y. Cheng, and Y. Qin, "Sparse bayesian perspective for radar coincidence imaging with array position error," *IEEE Sensors Journal*, Vol. 17, No. 16, 5209–5219, 2017.
17. Li, D., X. Li, Y. Cheng, Y. Qin, and H. Wang, "Radar coincidence imaging in the presence of target-motion-induced error," *Journal of Electronic Imaging*, Vol. 23, No. 2, 023014, 2014.
18. Jiang, Z., Y. Guo, J. Deng, W. Chen, and D. Wang, "Microwave staring correlated imaging based on unsteady aerostat platform," *Sensors*, Vol. 19, No. 12, 2825, 2019.